Enhanced interface perpendicular magnetic anisotropy in electrodeposited Co/Au(111) layers

L. Cagnon,[1] T. Devolder,[2] R. Cortes,[1] A. Morrone,[3] J. E. Schmidt,[3] C. Chappert,[2] and P. Allongue[1,*]

[1]*Laboratoire de Physique des Liquides et Électrochimie (CNRS UPR-15), Université P & M Curie, 4 Place Jussieu, Tour 22 E5, F-75005 Paris, France*

[2]*Institut d'Électronique Fondamentale (CNRS UMR 8622), Bât. 220, Université Paris-Sud, F-91405 Orsay, France*

[3]*Laboratório de Magnetismo, Instituto de Fisica-UFRGS, 91501-970 Porto Alegre, RS, Brazil*

(Received 16 August 1999; revised manuscript received 17 July 2000; published 20 February 2001)

This work investigates the structure and interface perpendicular magnetic anisotropy (PMA) of electrodeposited Cu/Co/Au(111) sandwiches with variable Co thickness [2–20 monolayers (ML's)]. In optimum deposition conditions, polar magneto-optical Kerr effect measurements show that the axis of easy magnetization is perpendicular to the layers for thicknesses below ca. 7.2 ML's. This value is among the best ever reported for the Cu/Co/Au(111) structure. While extended x-ray-absorption fine structure indicates that layers are hcp, *in situ* STM imaging suggests that magnetoelastic effects contribute significantly to PMA. The correlation observed between the strength of PMA and film structure is discussed in details.

DOI: 10.1103/PhysRevB.63.104419 PACS number(s): 75.70.Ak, 81.15.Pq, 75.30.Gw, 68.55.−a

I. INTRODUCTION

Tailored two-dimensional (2D) nanostructures $M/F/M$, with M a noble metal and F an ultrathin ferromagnetic layer, have been intensively studied over the last decade for their specific magnetic properties such as perpendicular magnetic anisotropy (PMA).[1–4] PMA is indeed of considerable interest for high-density data storage.[5] Out-of-plane magnetization has been reported with UHV or sputter-grown Co/Au(111) sandwiches and multilayers.[1,4–6] Single crystals and thin films of gold, evaporated, or sputtered on float glass, mica, or Cu/Si(111) substrates were successfully used.[7–9] Electrodeposition was also used recently.[10] Optimization of the preparation techniques has been critical to achieve perpendicular anisotropy. One important advantage of electrodeposition is perhaps the easy control of nucleation and growth modes by fine adjustment of the deposition potential and solution chemistry.[11,12] For instance, giant magnetoresistance was achieved with magnetic alloys and multilayers, deposited from a single bath.[13–16]

This study shows that electrodeposited Cu/Co/Au(111) layers exhibit strong perpendicular magnetization. PMOKE (polar magneto-optical Kerr effect) characterizations indicate that *out-of-plane* magnetization is obtained at any potential of deposition and below a critical cobalt thickness t^*. Perfectly square hysteresis loops with coercive forces up to ~0.5 kOe were measured below t^*. The optimum t^* value of ~7.2 monolayers (ML's) is greater than the best ones ever reported for the Co/Au(111) interface, either prepared by molecular beam epitaxy (MBE) or sputtering. To explain this behavior we show, using *ex situ* EXAFS (extended x-ray-absorption fine structure) and *in situ* scanning tunneling microscopy (STM), that layer by layer (0001)Co/Au(111) epitaxial growth occurs. Correlation between structural characterizations and PMOKE are used to estimate the different contributions to PMA. Comparison is made with MBE layers.

II. EXPERIMENT

Cobalt layers were electrodeposited on 100-nm-thick gold films evaporated on freshly cleaved mica substrates. Au films were flame annealed and cooled down in air before use. Figure 1 shows the typical morphology of Au substrates imaged by atomic force microscopy (AFM). X-ray diffraction (XRD) indicates that the grains are (111) textured [full width at half maximum (FWHM)=0.5°] and aligned in plane with respect to the lattice of mica (FWHM=7°). While deep defective regions separate submicrometer wide grains (dark regions in the image), the top of the grains is nearly atomically flat and STM imaging will show the usual $22\times\sqrt{3}$-surface reconstruction of Au(111) after flame annealing (see below). The electrochemical response of such a sample was correspondingly quasi identical to that of an Au(111) single-crystal electrode.

Electrochemical experiments were conducted with a three-electrode cell, with a saturated mercury sulfate

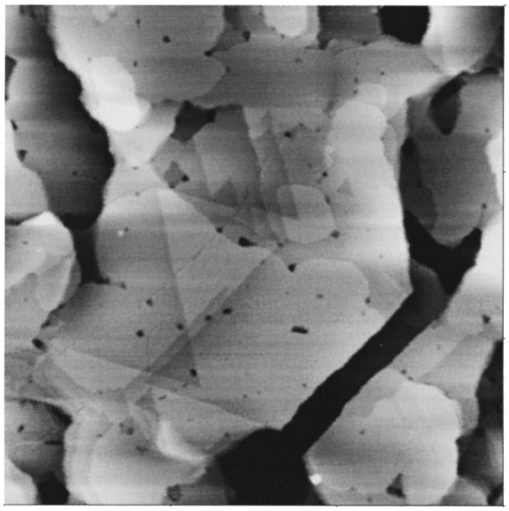

FIG. 1. ($1.5\times1.5\,\mu$m) AFM image of (111) textured Au/mica film after flame annealing. The gray scale is 3 nm from white to black.

Hg/Hg_2SO_4 electrode as reference of potential. *In situ* STM was performed using a home-built microscope.[17] Electrochemically etched tungsten tips were employed. They were insulated with Apiezon wax to reduce the electrochemical current. A Pd wire, loaded with hydrogen by reducing protons for 30 min, served as quasireference electrode. All potentials are quoted versus the Hg/Hg_2SO_4 electrode after control of the potential of the Pd-H electrode before and after the STM experiment.

Ex situ EXAFS was performed at the synchrotron facility at LURE (Orsay), using line D21 with a beam energy of 1.85 GeV. Data were collected with a two flat Si(311) single-crystal monochromator. Harmonics were rejected by using a grazing incidence mirror with a cutoff at 10 keV. Experiments were conducted in fluorescence mode and the signal at Co K edge (7.709 keV) recorded. The resolution is estimated to be ~ 2 eV. To improve the signal-to-noise ratio, the x-ray beam impinged the sample at a grazing incidence $<1°$, which is smaller than the critical angle for total reflection on Au. The beam polarization was out of plane ($E_\perp$).

Hysteresis loops (HL's) were recorded using a custom PMOKE setup (applied field perpendicular to the film, at light wavelength 632.8 nm).[7] The Co thickness of studied samples was precisely determined after deposition by Rutherford backscattering (RBS) using the 2-MeV Van Graaff accelerator of the Groupe de Physique des Solides (Université Paris 7).

III. RESULTS

A. Electrochemical characterizations and sample preparation

Figure 2(a) presents the electrochemical response of an Au(111)/mica sample in the 1-mM $CoSO_4$ solution as well as in the supporting electrolyte, which consisted in 10 mM K_2SO_4+0.1 mM KCl+1 mM H_2SO_4. The reduction of Co^{2+} is identified by the cathodic wave at -1.3 V. The wave at -1.15 V, observed in the two solutions, corresponds to the reduction of protons. The positive peak around -0.75 V is related to stripping of Co. Integration of this peak was used to estimate the deposition rate, assuming that the associated charge is uniquely related to the reaction $Co \rightarrow Co^{2+} + 2e^-$. Deposition of 1 ML of (0001)Co (in plane atom density of $1.85 \times 10^{15}/cm^2$), corresponds to a charge $Q_{ML} = 0.59\,mC/cm^2$. In what follows deposition will be either defined by the applied bias U or by the overpotential $\eta = E_0[Co^{2+}/Co] - U$ ($\eta > 0$), where $E_0[Co^{2+}/Co] = -1.03$ V is the Nernst potential. The estimated growth rates are 0.17 ML/s at $U = -1.6$ V ($\eta = 0.57$ V) and 0.06 ML/s at $U = -1.3$ V ($\eta = 0.27$ V).

The above deposition rates served, however, only as guide to prepare final samples. For accurate correlation between thickness, structure, and magnetic characterizations, the Co thicknesses t were precisely measured *a posteriori* using RBS. Figure 2(b) presents an example of RBS result obtained with a Cu/Co/Au(111) trilayer (the deposition procedure is described in the next paragraph). The most prominent features are related to the Au film ($1.87 < E < 2$ MeV) and mica substrate (series of plateaus at $E < 1.37$ MeV). The small peaks around 1.72 MeV are related to Co and Cu (see inset). After deconvolution and integration of peaks, the Co atom density was converted into an average Co thickness, assuming the (0001)Co structure [one monolayer is 2 Å thick or 1.85×10^{15} atoms/cm^2]. Notice that we take advantage of the small thickness of Au films to dose elements with atomic numbers *smaller* than that of Au.

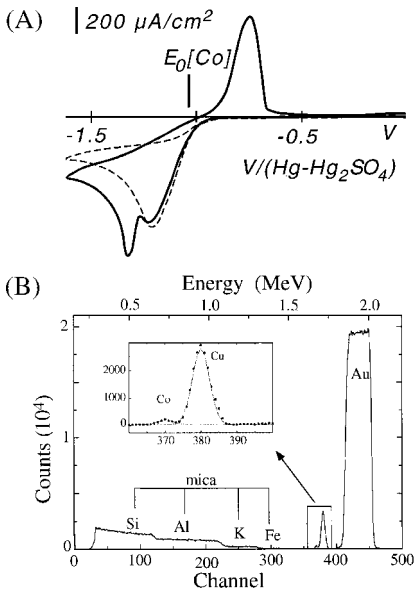

FIG. 2. (a) Cyclic voltammograms of Au(111) in a 1 mM $CoSO_4$ solution (solid line) and supporting electrolyte (dashed line). Scan rate: 50 mV/s. Supporting electrolyte: 10 mM K_2SO_4 + 0.1 mM KCl + 1 mM H_2SO_4. (b) Typical RBS spectrum for a Cu/Co/Au(111) trilayer on mica. Elements are indicated in the figure.

For *ex situ* EXAFS and PMOKE measurements, the Co/Au(111) films were capped *in situ* by a Cu layer to prevent air oxidation of the Co layer. The following procedure was used. (i) The Au sample was immersed at $U = -0.9$ V to keep the surface reconstructed. (ii) Co deposition was initiated by applying the desired potential (overpotential η). (iii) To stop deposition the potential was rapidly set to $U = -1.15$ V where neither dissolution nor deposition occurs. (iv) Last, the sample was capped with ~ 70 ML's of Cu by *adding* few drops of a 10-mM $CuSO_4$ solution to the cobalt bath. This procedure avoided any transfer of the Co layer through air and proved to efficiently protect the Co layer since PMA remains stable over months.

B. PMOKE characterization of Cu/Co/Au(111) sandwiches

The choice of a Cu-capping layer was primarily imposed by electrochemical considerations. Cu presents the immense advantage that it may easily be deposited from the same supporting electrolyte used for Co deposition. To prepare symmetrical Au/Co/Au sandwiches, the Co layer should have been transferred into a cyanide solution of elevated pH.[11] The second advantage of Cu is the very weak PMA at the Cu/Co interface.[7] The strength of PMA at the Cu/Co/Au(111) sandwich will thus be mostly correlated to the Co/Au interface and the Co film inner structure.

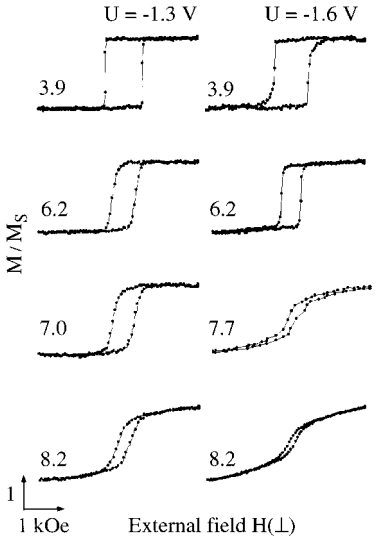

FIG. 3. Normalized PMOKE hysteresis loops obtained with electrodeposited Cu/Co/Au(111) layers. Co deposits were grown at −1.3 V (left) and −1.6 V (right). The figures attached to loops is the Co thickness *t* expressed in atomic monolayers (ML's).

PMOKE hysteresis loops (HL's) are presented in Fig. 3. For normalization, the saturation magnetization M_S was measured at $H=15$ kOe. The figures associated to each HL are the Co thicknesses derived from RBS measurements and expressed in ML's. The left and right columns correspond to films grown, respectively, at $\eta=0.27$ and 0.57 V. Since PMOKE is exclusively arising from the component of the magnetization *M* normal to the surface, and the field *H* is applied perpendicularly to the films, square hysteresis loops (HL's) indicate that *M* is completely *perpendicular* for a thickness $t\sim 4$ ML's, irrespective of the deposition bias. The corresponding coercive field $H_C=0.5$ kOe is comparable to the values reported for evaporated films.[4] At a given bias, the coercive forces decrease with increasing Co thickness, while loops become more rounded, indicating that the mean easy axis of magnetization is tilting towards in-plane orientation. The influence of the deposition conditions are twofold: (i) With increasing *t*, the coercive force decreases faster for $\eta=0.57$ V than for $\eta=0.27$ V. (ii) for $t\sim 4$ ML's, the loop is perfectly square for $\eta=0.27$ V, while saturation is slower for $\eta=0.57$ V.

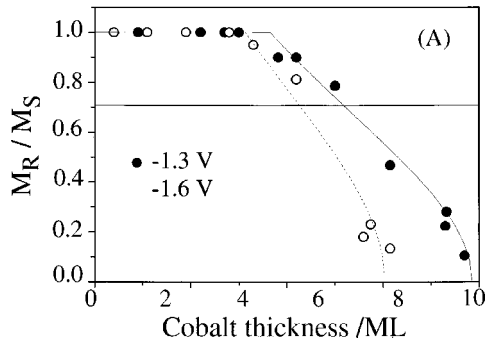

FIG. 4. (a) M_R/M_S vs *t* derived from PMOKE loops of Fig. 3, with M_S measured at applied field 15 kOe. The solid lines correspond to the plot of Eq. (A7) (see the Appendix, Procedure II). The deposition potential is −1.3 V (bold symbols) and −1.6 V (open symbols).

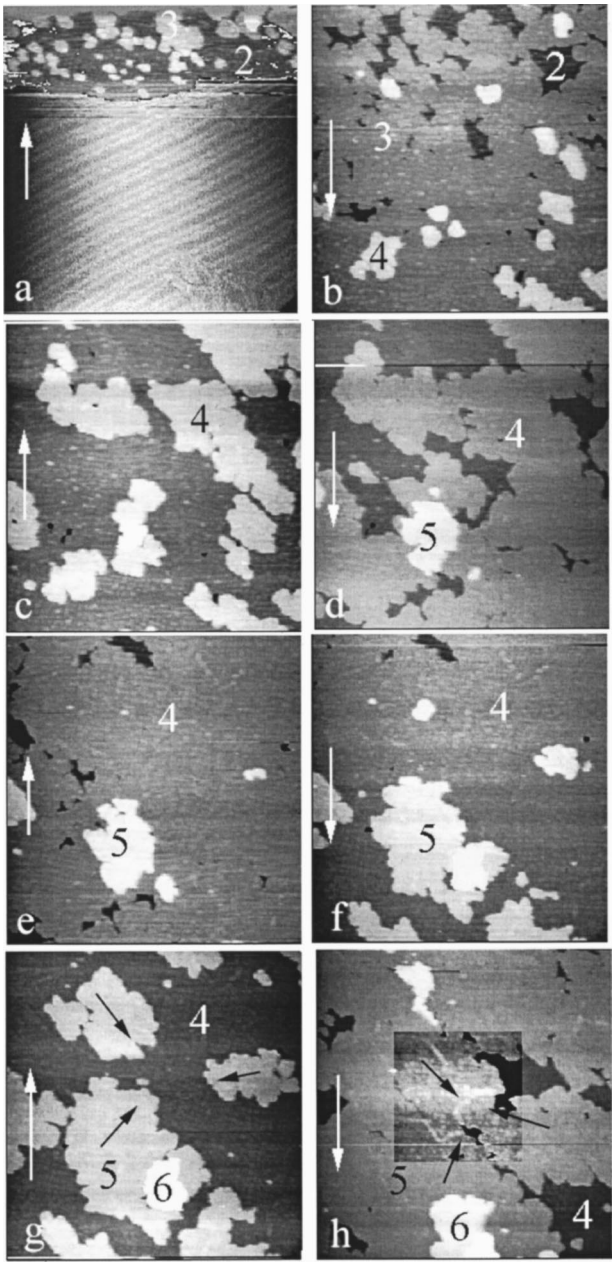

FIG. 5. Sequence of STM images showing 2D growth of Co on Au(111). The deposition potential was −1.3 V. In (a), bottom, $U=-0.9$ V. The (1250×1320 Å) frames were recorded 50 s apart. Vertical arrows give the direction of slow tip scanning. Figures *N* inside images are the local number of Co atomic monolayers. Note the smoothness of the layer. The contrast was enhanced in image (h) to show structural defects in the square box.

Figure 4 displays the variations of M_R/M_S vs *t*, where M_R is the remnant magnetization (measured at $H=0$). The solid lines are fitting curves using Eq. (A7) (see the Appendix). This curve represents also the variations of the angle θ between the magnetization axis and the surface normal since $M_R/M_S=\cos\theta$. The strength of PMA is generally character-

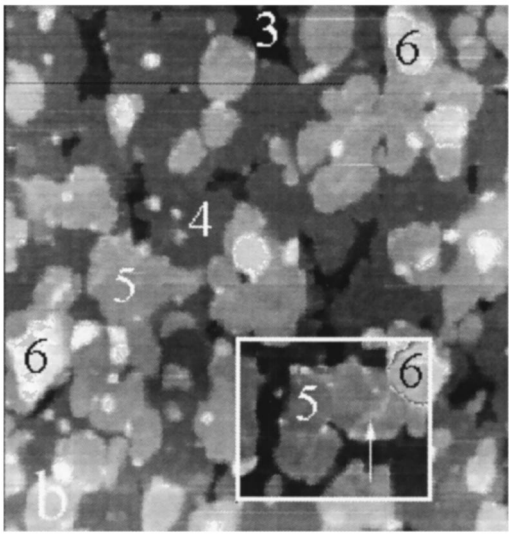

FIG. 6. 1260×1330-Å STM view of a 5-ML-thick Co layer grown at −1.6 V. The contrast was enhanced in the square boxes to show structural defects. This image must be compared to the last frame of Fig. 5. Figures *N* inside images are the local number of Co atomic monolayers.

ized by the critical thickness t^* for which $\theta = 45°$; we find that $t^* \sim 7.2$ ML's for $\eta = 0.27$ V and ~6.2 ML's for $\eta = 0.57$ V. These values are the largest ever reported for a Cu/Co/Au(111) structure.[4,7] The influence of the applied bias for deposition conditions is real and significant as will be discussed later on. We would like to report that alternating gradient-field magnetometery (AGFM) measurements (not shown) gave essentially the same results. The only difference was that AGFM loops are slightly more rounded than corresponding PMOKE square loops when $t < t^*$. This altered behavior is assigned to the fact that AGFM integrates the response over the whole sample surface, including the defects between grains (see Fig. 1), while PMOKE is less sensitive to such defective regions because they scatter the laser beam.

C. *In situ* STM observations

Figure 5 shows in real-time the growth of a cobalt layer at $U = -1.3$ V. The eight images were recorded within about 7–8 min (50 s/image). Vertical arrows indicate the direction of slow tip scanning. The figures *N* inside images are the local thickness expressed in atomic layers. In image (a), bottom, the surface is initially $22 \times \sqrt{3}$ reconstructed and Co growth is promoted at the top of the frame by stepping the potential from $U = -0.9$ to -1.3 V [upward tip scanning]. The straight front of growth indicates fast nucleation since the slow *y* axis represents also the time axis. A quasiperfect monolayer by monolayer growth then follows until the fifth atomic plane. Inside the box of image (h) the modified gray scale evidences some lines of contrast that are lighter than the remaining of the layer. These are domain boundaries arising from the coalescence of the three islands marked with black arrows in Fig. 5(g). As discussed below and elsewhere,[18] the first Co layer [top of image (a)] is *biatomic*

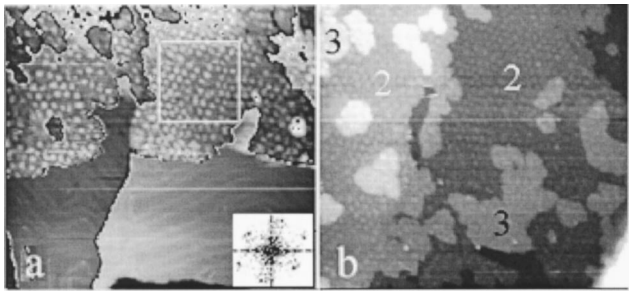

FIG. 7. Sequence of STM images showing the formation of the first three atomic planes of Co at $U = -1.3$ V. The potential was −0.9 V in the lower half of image (a). The (1000×900 Å) frames were recorded 50 s apart. A Moiré pattern is resolved on each layers; the 2D FFT spectrum in (a) corresponds to the region inside the square box.

($N = 2$). From this sequence, we conclude that the electrochemical growth processes are quite different from MBE growth modes where the nucleation is driven by the surface dislocations at elbows of the ''herring bone'' pattern of the reconstructed gold surface.[9,19–21]

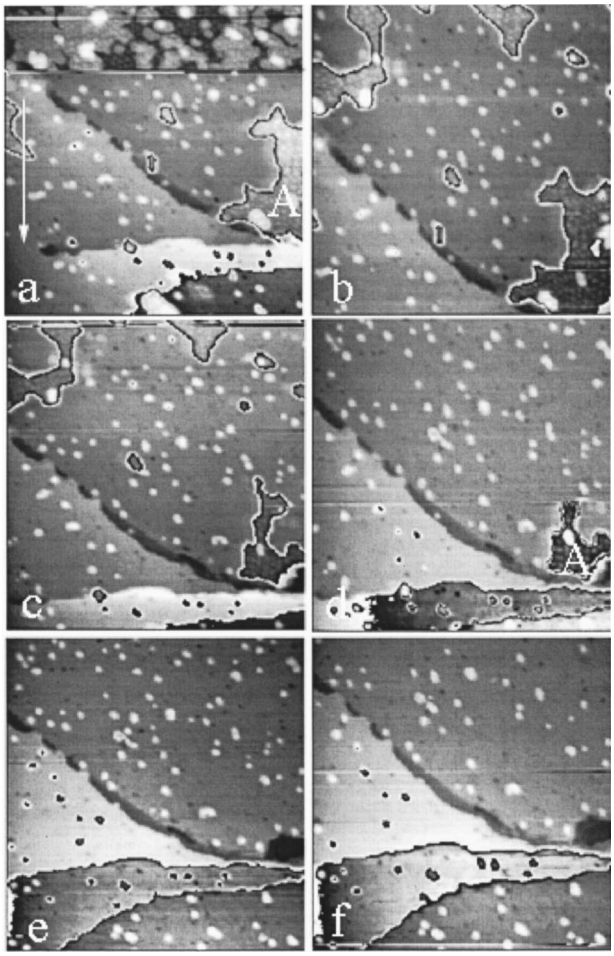

FIG. 8. Six-image STM sequence showing the dissolution of a 3-ML Co layer. The potential was $U = -1.3$ V in the top of image (a) and was stepped to −0.95 V. Note the nm islands left after stripping. Island (*A*) is biatomic. The (1150×1200 Å) frames were recorded 50 s apart.

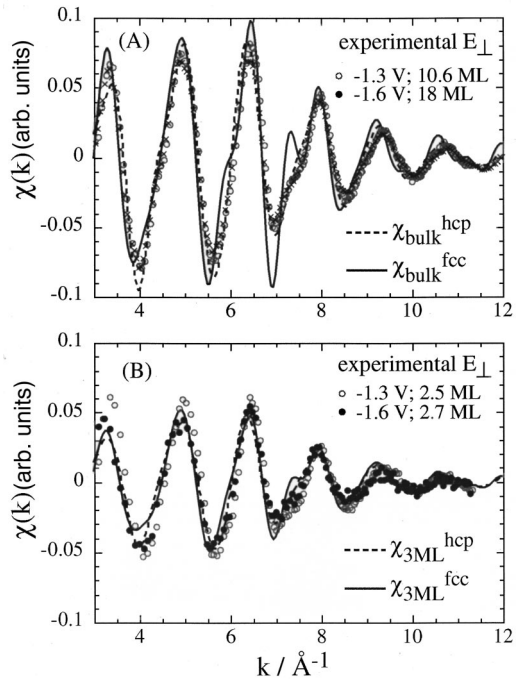

FIG. 9. EXAFS results with out of plane beam polarization. (a) experimental and theoretical $\chi(k)$ curves for thick layers ($\geqslant$10 ML's); (b) same but for thin layer ($\leqslant$3 ML's). The film thickness and deposition potential are indicated. Data points are experimental and solid or dashed lines are calculated ones. In the case of hcp Co calculation are performed with the *c* axis parallel to the beam polarization.

The influence of the overpotential on the film morphology was next studied. The ~5-ML-thick-film in Fig. 6 was grown at $\eta = 0.57$ V ($U = -1.6$ V). This morphology may be directly compared to the 5-ML-thick layer in Fig. 5(h) since the frames have the same size. Clearly, increasing η makes the Co grains smaller and more atomic layers are exposed to solution. Basically the film is rougher as the deposition rates increases. Some domain boundaries are again visible on top of grains; see for instance the lines of contrast inside the square box (arrow).

Figure 7 focuses on the early stages of the growth at $U = -1.3$ V. The potential was -0.9 V in the bottom image of (a) and stepped to -1.3 V in the middle of the frame [upward tip scanning]. The height of the first Co layer is 3.4 Å, a value that falls between the height expected for a monolayer (2 Å) and a bilayer (4 Å). This measure was nearly independent on the tunneling conditions (voltage and set point current). We therefore conclude that the first Co layer must be *biatomic* but that electronic effects are probably occurring. A (28 ± 1)-Å hexagonal Moiré pattern is also resolved on top of the bilayer; the 2D fast Fourier transform (FFT) spectrum in the inset of Fig. 7(a) corresponds to the region inside the square box. The peak to valley corrugation is ~0.42 Å. Looking at the initial surface reconstruction, one also notes that, locally, the close-packed row of the Moiré pattern are either 90° or 30° off the direction of domain walls of the Au(111) reconstruction, i.e., with respect to $\langle 11\text{–}2 \rangle$. In image (h) the bilayer is completed and islands of the next layer have nucleated. These correspond to the third atomic layer since islands are monatomic (2 Å). A Moiré is again resolved but its dimension reduces to (24 ± 1) Å; the corrugation decreases also (~0.25 Å). In other series the subsequent layers are all monatomic with an ill-defined Moiré (only occasionally observed) because the corrugation is less than ~0.1 Å.

TABLE I. Least-square fit in α of $\chi^n(k)k^2$ using the function $y(k) = \alpha\chi^{hcp}(k)k^2 + (1-\alpha)\chi^{fcc}(k)k^2$ with $\chi^{hcp,fcc}_{bulk}$ and $\chi^{hcp,fcc}_{3ML}$, respectively, the theoretical functions for thick ($\geqslant$10 ML's) and thin films ($\leqslant$3 ML's). $Chi^2 = \Sigma[y(k) - \chi^n(k)k^2]^2$.

U/V	Co thickness/ML	α	Chi^2
−1.3	10.6	0	52
		0.9	7.4
		1	7.9
−1.3	2.5	0	17
		0.97	9.0
		1	9.0
−1.6	18	0	48
		0.82	9.8
		1	11
−1.6	2.7	0	22
		0.88	14.7
		1	14.9

Figure 8 is a six-image sequence studying the dissolution of a Co layer. Dissolution was initiated by reversing the potential of the sample to $U = -0.95$ V in the upper quarter of Fig. 6(a) [downward tip scanning]. After only one frame, only few big 2D islands remain together with a huge population of nm-sized islands. The bigger islands slowly disappear along the sequence, e.g., island *A* (height 3.4 Å) completely disappears after five images [see Fig. 8(e)]. In contrast, the nm islands remain quite stable over a period of time that exceeds the duration of the sequence displayed (i.e., several minutes). About 90% of nm islands survived over the sequence. At a more positive bias their dissolution was however much faster. The characteristic dimension of nm islands were a height of (2 ± 0.1) Å and a mean apparent diameter of 2–3 nm. While these dimensions remained independent on the deposition conditions, a systematic influence of the overpotential was noticed on their density: $N_{islands} \sim 5 \times 10^{11}$ islands/cm^2 for $\eta = 0.27$ V and 1×10^{12}/cm^2 for $\eta = 0.57$ V. Given the electrochemical stability of gold (up to ~0.5 V) and the much faster dissolution of bulk cobalt for potentials $U > E_0(Co/Co^{2+})$, we will discuss that the nm islands are neither pure cobalt nor pure gold.

D. *Ex situ* EXAFS characterizations

Ex situ EXAFS was performed on Cu/Co/Au(111) structure to check whether electrodeposited Co layers are hcp or fcc. Literature reports indeed that the pH of the solution and applied overpotential are critical parameters.[22,23]

Figure 9 compares experimental $\chi(k)$ EXAFS signal to theoretical curves. Calculation were performed using the FEFF code[24] for out-of-plane beam polarization ($E_\perp$). In the case of films thicker than 10 ML's [Fig. 9(a)] experimental curves are compared to those calculated for bulk cobalt. A

TABLE II. Results of fit of first neighbor peak from EXAFS experiments. The last three lines correspond to simulations with 3-ML films under the same lateral stress ($\varepsilon_x = 2.5\%$) but with different vertical compressions ε_z. The effect of ε_x on $R_\perp$ value is visible when the compression ε_z deviates from expectations [$\varepsilon_z = -0.57\varepsilon_x$ (Ref. 34)]. $\text{Chi}^2 = \Sigma[\chi_{\text{theo}}(k)k^2 - \chi(k)k^2]^2$.

Conditions (U, t_{Co}, polarization)	$R_\perp$ (Å)	σ	N^*	Chi^2
−1.3 V, 10.6 ML's, $E_\perp$	2.493	0.094	10.86	0.032
−1.3 V, 2.5 ML's, $E_\perp$	2.480	0.104	9.84	0.072
−1.6 V, 18 ML's, $E_\perp$	2.490	0.092	11.28	0.013
−1.6 V, 8 ML's, $E_\perp$	2.489	0.093	10.79	0.036
−1.6 V, 2.7 ML's, $E_\perp$	2.481	0.107	8.65	0.03
Simulation				
$\varepsilon_z = -1.25\%$, $E_\perp$	2.501			
$\varepsilon_z = 0\%$, $E_\perp$	2.522			
$\varepsilon_z = -5\%$, $E_\perp$	2.418			

strong focusing effect occurs around $k \sim 7-8$ Å^{-1} in curve $\chi^{\text{fcc}}_{\text{bulk}}(k)$ due to the symmetry of the crystal. This effect is not observed in the case of $\chi^{\text{hcp}}_{\text{bulk}}(k)$ provided the beam polarization remains *parallel* to the *c* axis; with the beam polarization *normal* to the *c* axis the curve would resemble that of fcc Co. For 2–3-ML-thick films experimental data are compared to curves calculated for 3 ML's of cobalt with different stacking. A focusing effect in again observed in $\chi^{\text{fcc}}_{\text{3ML}}(k)$. Given the normal beam polarization, the comparison of experimental and theoretical curves indicates that our electrodeposited cobalt layers are hcp with the *c* axis normal to the surface since no focusing is seen. This is also consistent with the hexagonal symmetry of the Moiré seen in STM images.

The above results are *qualitatively* similar for deposits grown at −1.3 and −1.6 V. However, looking into more details, we found a systematic and significant influence of the overpotential on the crystallographic quality of Co layers. We performed least-square fits of the experimental function $\chi^n(k)k^2$ with the theoretical function $y(k) = \alpha\chi^{\text{hcp}}_{\text{bulk}}(k)k^2 + (1-\alpha)\chi^{\text{fcc}}_{\text{bulk}}(k)k^2$. The suffix *n* means that the experimental signal was multiplied by the factor $N/(N-1)$, with N the average film thickness expressed in ML's, to normalize the amplitudes of curves and suppress the effect of the thickness.[25] α is a parameter quantifying the volume fraction of Co atoms in hcp surrounding. For 3-ML films, the procedure used theoretical curves $\chi^{\text{hcp}}_{\text{3ML}}(k)$ and $\chi^{\text{fcc}}_{\text{3ML}}(k)$ functions. Table I collects the α values. The hypothesis of pure fcc Co (i.e., $\alpha = 0$) always yields a fit quality far worse than with for pure hcp Co ($\alpha = 1$). The fit is significantly improved by introducing the variable α. Numerically α is as large as 0.97 for 3 ML's and slightly decreases to 0.9 for 10 ML's at the optimum potential of −1.3 V. For $U = -1.6$ V, α reduces to 0.8. This suggests that the density of defects increases with the overpotential.

Finally, Table II gives the nearest neighbor distance $R_\perp$, the Debye-Weller factor and the effective number of next neighbor N^* derived from the fit of the peak of first neighbors (the suffix $\perp$ refers to out-of-plane beam polarization). Experimentally, only slight variations of $R_\perp$ with film thickness are found. Values remain quite close to expectations and are consistent with previous determinations.[26]

IV. DISCUSSION

A. Structural properties of Co layers

Crystallographic structure. EXAFS indicates that our electrodeposition (ED) Co/Au(111) layers have a quasiperfect hcp structure from the very early stages of the growth [Figs. 9(a) and 9(b) and Table I]. The *c* axis is most certainly perpendicular to the surface because there is no focusing effect with $E_\perp$. This is also consistent with the hexagonal symmetry of the Moiré in STM images. There is a significant

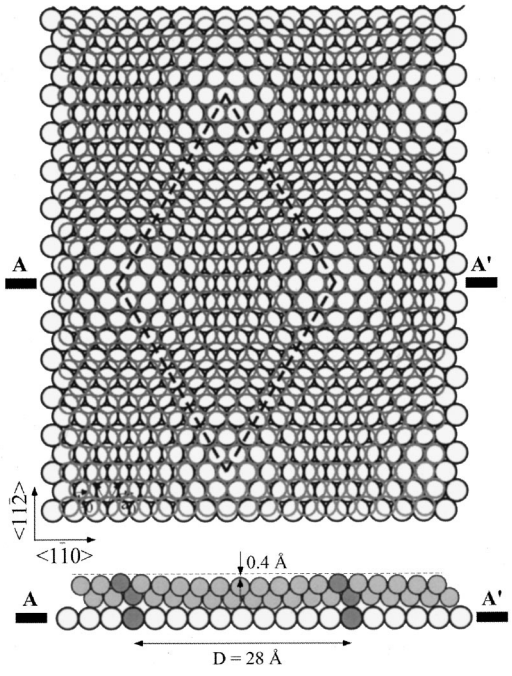

FIG. 10. Atomic model for the Co bilayer (top and side view). The hexagonal Moiré ($D = 28$ Å) is referenced with respect to the Au(111) lattice and it is assumed that the two Co planes have the same lattice parameter.

effect of applied bias from Table I. For $\eta = 0.27$ V, which corresponds to optimum conditions, the film grows perfectly hcp up to 10 ML's. By comparison structural defects are created by growing the films faster at $\eta = 0.57$ V. Possible candidates as defects are fcc stacking faults and also the domain boundaries seen Figs. 5(h) and 6. Deposition conditions have also an impact on the film roughness since Co layers become rougher as η increases [Figs. 6 and 5(g)].

Interface alloying. The electrochemical stability of the nm islands ($N_{\text{islands}} \sim Cst$ over the sequence in Fig. 8) at a bias which is 80 mV *positive* of the Nernst potential $E_0[\text{Co/Co}^{2+}]$ is quite surprising. At -0.8 V N_{islands} would decay faster (not shown). The stability of the nm islands towards dissolution is far worse than that of gold, which is electrochemically much more stable (up to $U \sim 0.5$ V). It is far better that of Co, which is highly unstable as soon as $U > -1.0$ V [see Fig. 2(a)]. From this we infer that the nm islands are neither pure cobalt islands nor gold islands and suggest that they are a mixture of Au and Co atoms resulting from local alloying. This hypothesis is consistent with the height $\sim 2 \pm 0.1$ Å of islands, a value which falls between the height of Au monatomic islands (2.35 Å) and of Co monatomic layer on Au (1.7 Å).[18]

Interfacial stress. The occurrence of elastic stress in electrodeposited layers has been often reported in literature. For instance, Cu electrochemical growth leads to pseudomorphic layers, on Au(100) and Pt(100).[27,28] While strain relaxation occurs for 1–2-ML thickness in vacuum, the phenomenon is observed above 5–10 ML's in the electrolytic environment. This remarkable difference is generally attributed to anion adsorption[27,28] because it promotes compressive strains.[29] Anions (in our case SO_4^{2-}, Cl^-) are indeed bigger than atoms and strongly interact with the surface, which helps in keeping surface atoms of the deposit apart from each other. Anion adsorption is therefore thought to be a source of stabilization of internal tensile stress.

The characteristic dimension D of the Moiré pattern was used to determine the internal strain (see Fig. 10). Since there is no rotation of the hexagonal pattern with respect to the gold lattice we simply used the classical formula for D,[30] under the hypothesis that all Co atomic layers have the *same* lattice constant. Unstrained layers would therefore promote a Moiré with $D \sim 20$ Å which is far smaller than experimentally measured. For $D = 28$ Å (case of the bilayer) one finds a Co-Co distance of 2.61 Å and a tensile stress $\varepsilon_x = +4\%$. For $D = 24$ Å, case of the trilayer, Co-Co $= 2.57$ Å or $\varepsilon_x = +2.5\%$. The absence of a clear Moiré on subsequent atomic layers suggests either the formation of atomic planes that are keeping the same stress of 2.5% for $N \geqslant 4$ or that atomic layers are essentially relaxed on top of a 2.5% stressed trilayer. In the later hypothesis a residual stress of 1%, i.e., Co-Co $= 2.53$ Å, would promote $D \sim 100$ Å. For a completely relaxed layer $D \sim 200$ Å. Both cases are probably difficult to distinguish because such patterns would be rather difficult to resolve by STM by lack of order. We also considered the assumption that the first three atomic layers had not the same lattice parameter (contrary to Fig. 10). This eventuality was rejected since it conflicts with the experimental decrease of the D parameter upon deposition (D should increase).

Under the assumption of Fig. 10, the estimate of ε_x shows that the elastic energy, which scales as $[N\varepsilon_x^2]$, progressively reduces upon growth (N is the number of atomic planes deposited). The initial lattice mismatch being 14%, this calls for some mechanisms of strain relief. We propose that interface alloying (see above) is the result of the (partial) strain relief because Co and Au should not mix at room temperature.[31] Intuitively incorporation of ''big'' atoms from the substrate (Au) into a stressed layer (Co) certainly reduces eventual tensile strain. This simple model is supported by our own observations in the case Ni electrodeposition on Au(111).[32] In that case no nm island are left upon Ni stripping while the first Ni monolayer is totally unstrained.

Considering that alloying should initiate at domain boundaries at the Co/Au interface, the strain release must become easier as the density of grain boundaries increases. This expectation is in perfect agreement with the observation that N_{islands} increases with increasing η, i.e., as the density of Co nuclei increases (see Fig. 6). Therefore we conclude that interface alloying comes into support of a residual interface stress.

There is, however, an apparent contradiction between the conclusion derived from EXAFS and STM since the distance $R_\perp$ is too weakly thickness dependent and remains very close to expectations (see Table II). To lift this discrepancy, we calculated EXAFS spectra (with $E_\perp$) for films having an in-plane stress $\varepsilon_x = 2.5\%$ and different vertical elastic compressions ε_z. Results are given in Table II in the last three lines. They clearly indicate that the in-plane stress has *no consequence* on $R_\perp$ provided the compression follows the bulk relationship $\varepsilon_z \sim -0.57\varepsilon_x$.[34] $R_\perp$ becomes stress dependent when ε_z significantly deviates from the above relationship. Numerically there must be a compensation of the contribution of the different in-plane (elongated) and out of plane (compressed) Co-Co bonds. Calculation with in-plane beam polarization ($E_\parallel$) show, by contrast, that $R_\parallel$ depends on in-plane stress. Work is planned to perform corresponding measurements with $E_\parallel$. The ratio $R_\perp/R_\parallel$ will directly give the in-plane stress if one accounts for the fact that $R_\perp/R_\parallel = 1.003$ for bulk (0001) Co (see Ref. 30, page 76, $a = 2.501$ and $c = 4.066$).

We would like to make a comment on the huge compression of the bilayer, as measured from STM observations. This height, which is -15% smaller than anticipated from a hard sphere model even if one accounts from the -2.3% plastic compression ($\varepsilon_z = -0.57\varepsilon_x$). The discrepancy stems from the fact that it is measured with respect to the *naked* gold surface. In other words this height is *apparent* and local variations of the tunneling barrier between the naked gold and the Co layer must be considered.[37] Note that the measured height of next cobalt monolayers (2 Å) is consistent with expectations since one measures it with respect to the Co film.

One question relevant to PMA is the persistence of the stress upon Co growth. The fact that the fourth atomic layer is nearly relaxed insures that further Co deposition will not

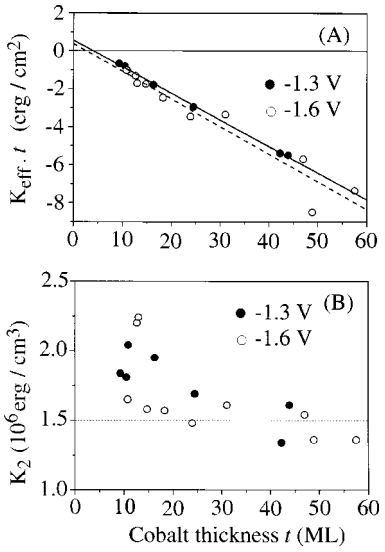

FIG. 11. Parameter determination using Procedure I: (a) Variations of $K_{\mathrm{eff}} \times t$ vs t. Straight lines are least-square fits. (b): Variation of K_2 vs t. The potential of deposition is -1.3 V (solid symbols) and -1.6 V (open symbols).

affect the residual interface stress. In the case of thick films, the Cu capping will have no effect because the distance Co-Co on top of the third atomic layer (2.57 Å) and the expected Cu-Cu distance [2.56 Å for Cu(111)] are almost equal. The question might become critical on a bilayer film.

B. Magnetic state of Cu/Co/Au(111) sandwiches

For a Co thickness t well below t^*, the situation is simple. For $\eta = 0.27$ V, HL's are almost perfectly square with fully out-of-plane magnetization. This is typical of a reversal mode involving a few nucleation events occurring at similar field values, followed by easy domain-wall propagation. The sample is highly uniform and the domain walls sweep rapidly the entire surface of the sample. For $\eta = 0.57$ V, HL's are rounded near saturation (but not upon reversing magnetization). The slow saturation can be tentatively attributed to a larger film roughness (see Fig. 6), which induces hard pinning centers for the domain walls, or leaves hard magnetic areas (those with low t).

For Co thicknesses t well above t^*, the magnetization reversal becomes mainly reversible. The differences in magnetic properties could also arise from the roughness of the Co layer. According to Fig. 4, a roughness of ± 1 ML is sufficient to promote the coexistence of adjacent portions of the Co layer exhibiting either out-of-plane or in-plane anisotropy. If the lateral size of Co terraces is larger than the expected width of domain walls (4–10 nm), then Co terraces can have their own *local* magnetization orientation. This results in complex averaged HL's near t^*, more rounded than expected for perfectly flat films. This could explain the rounded shape of the HL's of Fig. 3 at large Co thickness, especially for samples grown at $\eta = 0.57$ V.

The HL of the 8.2-ML film grown at $\eta = 0.27$ V ($M_R/M_S = R \sim 0.4$) may, for instance, be decomposed into HL's of regions of different thicknesses. A film made of regions which are 7 ML's ($R \sim 0.74$), 8 ML's ($R \sim 0.55$), and 9 ML's ($R \sim 0.35$) thick and represent, respectively, 20, 30, and 50 % of the total surface would have a $M_R/M_S \sim 0.49$ and an average thickness 8.3 ML's. This is in close agreement with experimental values and STM images (Fig. 6).

Note that when the terrace size is smaller than the width of domain walls or comparable,[38] an extrinsic contribution to the fourth-order anisotropy constant K_2 is expected. It smoothens the transition region between fully perpendicular and in-plane easy magnetization axis.

1. Determination of anisotropy constants

Anisotropy constants were calculated using the usual development for hcp Co, recalled in the Appendix. It assumes that the magnetization vector is uniform throughout the whole film, and that Co films are continuous with the hcp c axis normal to the surface. The last two hypotheses are consistent with our STM and EXAFS results. Individual fits of the reversible part of HL's give anisotropy constants K_{eff} and K_2 for each sample. This first approach (procedure I, see the Appendix) is valid for thick Co films ($t > t^*$) magnetized in plane. Figure 11(a) plots $K_{\mathrm{eff}}\ t$ vs t. The linear fit yields the

TABLE III. Anisotropy constants of Cu/Co/Au(111) structures. Procedure I: Parameters K_1, K_2, and global $K_S = K_S^{\mathrm{Co/Cu}} + K_S^{\mathrm{Au/Co}}$ derived from Fig. 11. Procedure II: Parameters t^*, K_S, and $K_S^{\mathrm{Au/Co}}$ derived from Fig. 4. State of the art values of t^* or $K_S^{\mathrm{Co/Au}}$ obtained with different types of samples are also given. ED=electrodeposition.

	Procedure I			Procedure II[a]		
Deposition potential	K_1 (erg/cm^3)	K_2 (erg/cm^3)	K_S (erg/cm^2)	t^* (ML)	K_S (erg/cm^2)	$K_S^{\mathrm{Au/Co}}$ (erg/cm^2)
-1.3 V	5.6×10^6	$1.6\pm0.2\times10^6$	0.57 ± 0.06	7.2 ± 0.2	0.78 ± 0.02	0.72 ± 0.02[b]
-1.6 V	$5.2\pm0.4\times10^6$	$1.5\pm0.2\times10^6$	0.38 ± 0.48	6.2 ± 0.2	0.72 ± 0.02	0.66 ± 0.02[b]
bulk Co (Ref. 29)	4.5×10^6	1.5×10^6				
Au(111)/Co/Cu (MBE) (Ref. 7)	5.8×10^6	1×10^6	0.45 (annealed)	6.6	0.64	0.58[b]
Au/Co/Au (sputtering) (Ref. 35)	4.9×10^6	1×10^6				
Au(111)/Co/Cu (ED) (Ref. 10)				0 to 7.4		

[a]Values derived from the fit of curves in Fig. 4 using Eq. (A7) (see the Appendix for more details).
[b]Calculated assuming $K_S^{\mathrm{Co/Cu}} = 0.06$ erg/cm^2 (Ref. 7).

slope $[K_1 - 2\pi M_S^2]$ and the offset $K_S = K_S^{Co/Cu} + K_S^{Co/Au}$. Using bulk Co value for M_S gives $K_1 = 5.6 \times 10^6$ erg/cm^3. For samples grown at $\eta = 0.57$ V the dispersion of K_{eff} values is too large to allow a precise numerical fit. However, the slope does not look very different from that for samples grown at $\eta = 0.27$ V (a fit actually gives $K_1 = 5.2 \pm 0.4 \times 10^6$ erg/cm^3). This large dispersion could be related to a fluctuation of roughness amplitude or stacking fault density, which could be very sensitive to minute changes in deposition conditions at large overpotential. Figure 11(b) shows that K_2 is not very much dependant on Co thickness and overpotential, and stays around the bulk value of 1.5×10^6 erg/cm^3. The slightly higher values for low Co thicknesses ($\sim$10 ML's) are attributed to an increasing influence of local anisotropy fluctuations,[38] as discussed above, and not to an intrinsic surface contribution to K_2.

Procedure II (see the Appendix) makes use of Fig. 4(a) and is relevant to thin samples ($t \sim t^*$). The variations $M_R/M_S = f(t)$ are fitted according to Eq. (A7), where $K_S = K_S^{Co/Au} + K_S^{Co/Cu}$ is kept as the main adjustable parameter, while values of K_1 and K_2 are chosen within the error bars of the parameters derived from procedure I for thick samples.

2. Anisotropy constants

Values are collected in Table III. *A priori*, procedures I and II are complementary. Procedure I is accurate to determine *volume* constants and procedure II accurate to determine *interface* parameters. This partly explains the lack of precision in the determination of K_S using procedure I, especially for $\eta = 0.57$ V (see Table III). The film roughness (Fig. 6) is thought to be a major source of inaccuracy because this complicates the magnetic behavior of layers. For these reasons the discussion focuses, on the one hand, on the value of the volume constant K_1 and K_2 derived from procedure I and, on the other hand, on the interface constant K_S derived from procedure II.

Volume constants K_1 and K_2. The experimental constant K_1 is $\sim$20% larger than the usual value for hcp Co,[36] which can be explained in terms of strains in the film, in agreement with structural characterizations. The value of K_2 is also consistent with bulk values.

Interface constant K_S. The highest value ($K_S = 0.78$ erg/cm^2) is observed for $\eta = 0.27$ V, which is also the optimum potential from the morphology viewpoint (Fig. 6). So far the best value of $K_S = 0.64$ erg/cm^2 was obtained with Cu/Co/Au(111) structures grown by MBE.[7] The comparison with other physical methods is even more favorable: sputtered Au/Co/Au sandwiches exhibit $K_S = 0.45$ erg/cm^2 *after* thermal treatment[39] and $K_S = 0.1$ erg/cm^2 without annealing. More generally, referring to the other data,[4] the strength of PMA obtained in our work is always higher than the one obtained by other physical methods. In another study, similar figures were reported if Co was electrodeposited at an overpotential of $\eta = 0.57$ V,[10] while PMA was not reported for $\eta = 0.27$ V.

Comparing the critical thickness t^* leads to the same conclusion. This parameter, which is most relevant for applications, presents the advantage of being free of any mathematical treatments of data. It is purely experimental. We obtain $t^* = 7.2$ ML's against 6.6 by MBE.

C. Contributions of PMA at ED Cu/Co/Au(111) layers

The reduced symmetry of the Co crystal at surface and interfaces generates some magnetic anisotropy energy. *Ab initio* calculation suggest that Néel's theory is incomplete or too simple to account for all observations.[40–42] The electronic structure of the ferromagnetic atoms is highly influenced by their hybridization with atoms from the substrate. At surfaces the trend is an enhancement of the spin moments due to reduction of the coordination number (the *d* band is narrower). However, other effects like interface roughness, magnetostriction, etc., may also come into play. These are estimated below in light of the structural information gained. The discussion will mainly focus on the K_S value derived from Fig. 4.

Effect of interface roughness. The effect of interface roughness is twofold. By changing the Co coordinence, it reduces the Néel-type anisotropy, that arises from local symmetry breaking. By altering the 2D shape of the layer, it lowers the shape anisotropy. The roughness of the Cu/Co interface being much larger than that of the Co/Au one, the influence of the latter may be neglected. An estimate of the variation of the Néel-type interface anisotropy[43] yields $\Delta K_S^{Co/Cu}/K_S^{Co/Cu} = -2\sigma/\xi$, where σ is the height of steps and ξ the mean lateral size of flat terraces. This effect is negligible in our case. With $\sigma = 2$ Å, $\xi = 140 - 120$ Å at the Co/Cu interface and assuming $K_S^{Co/Cu} = 0.06$ erg/cm^2,[7] one finds $\Delta K_S^{Co/Cu} = -2 \times 10^{-3}$ erg/cm^2.

The change in shape anisotropy is given by $\Delta K_S^{dip} = +(3\sigma/4)\ 2\pi M_S^2\ [1 - f(2\pi\sigma/\xi)]$, where $f > 0$ is a quickly decreasing function tabulated by Bruno *et al.*[44] Qualitatively the film roughness reduces the shape anisotropy and thus favors PMA. Taking the same value for σ and ξ yields $f = 0.84$ and $\Delta K_S^{dip} \sim \pm 0.01$ erg/cm^2. This is again negligible. Thus interfacial roughness does not significantly affect PMA in our samples.

Magnetoelastic effects. Several models have been developed. The one in Ref. 6 leads to a $1/t$ dependence of the total anisotropy when the layer is uniformly strained throughout the whole thickness. It can easily be generalized to layers where the stress is limited to the first few ML's before relaxation occurs. The magnetoelastic energy per unit volume of a *fully* coherent layer is given by $\delta E_{me}^{coh} = (\frac{3}{2})\ \lambda E_y \varepsilon/(1 + q t/t_{sub}) \sin^2\theta$,[4] which reduces to $(\frac{3}{2})\lambda \varepsilon_x E_y \sin^2\theta$ since the substrate thickness $t_{sub} \gg t$. In this expression, λ is the magnetostriction coefficient, E_y the Young modulus, $\varepsilon = (a_{bulk} - a_{layer})/a_{bulk}$ is the in-plane stress in the magnetic layer and q is the ratio of Young modulii of the layer and substrate. If the film is coherent until a thickness $t_C < t$, integration of δE_{me}^{coh} over the entire volume of the film yields $E_{me}^{coh} = (\frac{3}{2})\ \lambda \varepsilon E_y t_C/t$, which may be expressed as K_{me}^{coh}/t to show that the magnetoelastic contribution scales like an interface constant (see the Appendix). For a cobalt layer under *tensile* stress, $\varepsilon < 0$ and $\lambda < 0$; magnetoelastic effects are therefore favorable to PMA because $K_{me}^{coh} > 0$.

Referring to Sec. IV A, for films of thickness close to t^* (ca. 7 ML's) one must take $t_C \sim 3$ ML's or 6 Å and $\varepsilon = -\varepsilon_x = -2.5\%$ (according to the above definition $\varepsilon = -\varepsilon_x$). This yields $K_{me}^{coh} = 0.24$ erg/cm^2 or $\sim 0.33 \times K_S^{Co/Au}$ (see Table III) [the other parameters are bulk values for Co: $\lambda = -5 \times 10^{-5}$ and $E_y = 2.1 \times 10^{12}$ dyn/cm^2 (Ref. 36)]. This estimate is not very much depending on the choice of the t_C value since K_{me}^{coh} scales with $\sim \varepsilon t_C$ and the product $[N \times \varepsilon_x] \sim$ Cst for $N \leqslant 4$. With $t_C = 4$ Å and $\varepsilon = -4\%$ $K_{me}^{coh} = 0.35 \times K_S^{Co/Au}$. Magnetoelastic effects are therefore contributing quite significantly to the PMA at electrodeposited Co/Au(111) layers.

Bias dependence of PMA. The effect is small in terms of t^* (Fig. 4), but was systematically noticed. Looking in more detail, one remarks that η influences both the volume and interface constants K_1 and K_S (Table III). One may consider a reduction of stress as possible source of observations, because this hypothesis is consistent with the *simultaneous* decrease of both K_S and K_1. Numerically, a 1% reduction of ε_x is sufficient to account for the bias variation in K_S. This change of stress is difficult to verify experimentally from STM because domains are much smaller at -1.6 V than at -1.3 V (see Fig. 6). Nevertheless, the increased density $N_{islands}$ at -1.6 V qualitatively agrees with a reduction of internal strains (see discussion, Sec. IV A). This conclusion is also giving some positive feedback regarding the question of magnetoelastic effects at the Co/Au interface.

D. Comparison between ED and MBE Co layers

MBE Co growth on Au(111) is now a well-established process.[19–21] It occurs via formation of biatomic Co islands that nucleate at elbows of the ''herring bone'' reconstruction of the Au(111) surface. Islands grow laterally until percolation ($\sim$1.6 ML's) but grow 3D above 2 ML's. This results in very rough Co layers.

The question of the interfacial stress at the Co/Au(111) interface is rather confusing. From STM studies, Co biatomic islands must have a fairly *relaxed* structure since their height is 4 Å,[19–21] and the Moiré pattern is $\sim$20 Å.[21] An EXAFS study[26] agrees with this conclusion while x-ray surface diffraction[45] concludes to the existence of some stress (less than 1% of stress for 5–6 ML's). Reflection high-energy electron diffraction is the only method from which strong in-plane strains were detected.[46,47]

From a strict morphology viewpoint, one would anticipate that the strain relief is more favorable when the layer is composed of grains,[48] as is the case for Co MBE films, than when it is composed of wide 2D domains, as is the case with ED Co layers (see Fig. 5). This is due to the larger density of step edge atoms in the former case. We therefore postulate that, unlike for ED layers, K_{me}^{coh} must be negligible with respect to $K_S^{Co/Au}$ at MBE layers Co/Au(111).

Given the morphology of MBE Co layers, the main contribution to PMA is a reduction of the shape anisotropy induced by the roughness. To estimate this contribution we model Co films thicker than 3 ML's by a 146×75-Å rectangular array of grains which replicate the array of elbows of the $22 \times \sqrt{3}$ reconstruction.[49] The mean diameter of Co islands is taken as 105 Å (this diameter is the average of array edges) and the peak to valley corrugation is $2(N-2)$ Å since 3D islands percolate for $N \sim 2$ ML's. Within these assumptions and using the formalism above[43,44] one finds $\Delta K_S^{dip} = 0.20$ erg/cm^2 ($f = 0.64$) for a 5-ML film ($N = 5$, $\sigma = 6$ Å, and $\xi \sim 110$ Å). This value represent 35% of $K_S^{Co/Au}$ (Table III). The change in Néel type interface anisotropy induced by surface roughness is still negligible ($\Delta K_S^{Co/Au}/K_S^{Co/Au} = -10\%$ with the same parameters).

V. CONCLUSIONS

This study shows that electrodeposition is a versatile and powerful alternative to fabricate cheap and high quality magnetic nanostructures exhibiting strong PMA. Comparison between electrodeposited and MBE layers, suggests that ED layers exhibit even stronger PMA. Beside effects that are common to both types of interface (e.g., hybridization), we propose that reduced shape anisotropy could be a main factor favoring PMA in MBE layers while this is magnetoelastic effects at ED layers. Comparing different techniques of fabrication of magnetic nanostructures creates therefore an interesting synergy to elucidate a phenomenon like PMA.

ACKNOWLEDGMENTS

We thank M.-C. Bernard for RBS measurements on Cu/Co/Au layers. This work was partially supported by CNRS-Ultimatech and Capes/Cofecub 186/96 contracts.

APPENDIX: DETERMINATION OF INTERFACE ANISOTROPY COEFFICIENTS

Model

It is first assumed that the magnetization vector **M** is uniform over the film, and that the hcp *c* axis is normal to the film. Defining θ as the angle between the surface normal and **M**, θ at equilibrium is derived from minimizing the sum of all anisotropy contributions: dipolar (E_d), magnetocrystalline (E_{mc}), interface (E_S), and Zeeman (E_Z) energies, whose expressions are given below.

$$E_d = -2\pi \cdot M_s^2 \cdot \sin^2 \theta, \tag{A1}$$

$$E_{mc} = K_1 \sin^2 \theta + K_2 \sin^4 \theta, \tag{A2}$$

$$E_S = K_S \cdot \sin^2 \theta / t, \tag{A3}$$

$$E_z = -H \cdot M_S \cdot \cos \theta, \tag{A4}$$

where t is the cobalt thickness, M_S the saturation magnetization, H the applied magnetic field (perpendicular), and $K_S = (K_S^{Au/Co} + K_S^{Co/Cu})$ the total interface contribution. Negative terms tend to align **M** in the plane of the layer. Positive ones favor PMA. Minimization of total energy $E(\theta) = E_S + E_{mc} + E_d + E_z$ yields

$$K_{eff} + 2K_2 \sin^2 \theta = -H \cdot M_S / (2 \cos \theta), \tag{A5}$$

$$\text{where } K_{eff} = K_1 - 2\pi \cdot M_S^2 + K_S / t. \tag{A6}$$

Procedure I

The parameters K_{eff} and K_2 may be determined independently using a fit of the *reversible* parts of the PMOKE hysteresis loops (HL's). The method requires samples having *in-plane* magnetization with no perpendicular remnant component ($M_R=0$). It thus applies for sufficiently thick layers. For a given sample of thickness t, the magneto-optical hysteresis loop provides $M_\perp/M_S=\cos\theta$ as a function of H. From each point i of the loop, $Y_i=-H\times M_S/(2\cos\theta_i)$ and $X_i=2\sin^2\theta_i$ are calculated. Since $Y_i=K_{\text{eff}}+K_2X_i$ [see Eq. (A5)], the plot $Y_i(X_i)$ is a line whose intercept and slope yield respectively K_2 and K_{eff}. The above procedure is repeated for all samples, i.e., for different thicknesses t, to plot $K_{\text{eff}}\cdot t$ vs. t. As shown in Fig. 11, the result yields a line of slope $[K_1-2\pi M_S^2]$ and offset K_S.

Procedure II

For $H=0$, $\sin^2\theta=-K_{\text{eff}}/2K_2$ [see Eq. (A5)], therefore the curves M_R/M_S vs t in Fig. 4 may be used to derive K_S using $M_R/M_S=\cos\theta=\sqrt{}(1-\sin^2\theta)$. The following theoretical expression was used to fit the curve in Fig. 4.[7–8]

$$M_R/M_S=[1+(K_1-2\cdot\pi\cdot M_S^2+K_S/t)/(2K_2)]^{1/2}. \tag{A7}$$

A fit was first performed with the values of K_1 and K_2 given from procedure I and with K_S as input parameter. Since the slope of the decaying part of the curve was never correctly accounted, we slightly reduced K_2 from $1.5–1.6\times10^6$ to 1.45×10^6 erg/cm^2. It was checked that K_2 affects mainly the slope of the theoretical curve (in its decay region) while K_1 and K_S only influence the threshold thickness above which M_R/M_S deviates from zero. To determine K_S as a function of bias, the fit was therefore performed with the K_1 given in Table III and the same $K_2=1.45\times10^6$ erg/cm^2.

In the literature, the strength of PMA is often characterized by the critical thickness t^* for which the zero-field magnetization **M** is conical and makes an angle 45° with the surface normal ($M_R/M_S=1/\sqrt{}2$). Using Eq. (A7), t^* reads

$$t^*=K_S/(2\cdot\pi\cdot M_S^2-K_1-K_2). \tag{A8}$$

*Corresponding author. Email address: pa@ccr.jussieu.fr

[1] F. J. Himpsel, J. E. Ortega, G. J. Mankey, and R. F. Willis, Surf. Sci. Rep. **47**, 511 (1998).

[2] M. F. Doerner and R. L. White, MRS Bull. **21**, 28 (1996).

[3] T. Suzuki, MRS Bull. **21**, 42 (1996).

[4] W. J. M. de Jonge, P. H. J. Bloemen, and F. J. A den Broeder, in *Ultrathin Magnetic Structures*, edited by B. Heinrich and J. A. C. Bland (Springer-Verlag, Berlin, 1993), Vol. I, Chap. 1.3.

[5] M. Mansuripur, *The Physical Principles of Magneto-Optical Recording* (Cambridge University Press, Cambridge, England, 1995).

[6] C. Chappert and P. Bruno, J. Appl. Phys. **64**, 5736 (1988).

[7] P. Beauvillain, A. Bounouh, C. Chappert, R. Mégy, S. Ould-Mahfoud, J. P. Renard, and P. Veillet, J. Appl. Phys. **76**, 6078 (1994).

[8] R. Allenspach, M. Stampanoni, and A. Bischof, Phys. Rev. Lett. **65**, 3344 (1991).

[9] T. H. Gentner, T. Detzel, F. Scheurer, and J. P. Bucher, Thin Solid Films **275**, 58 (1996).

[10] J. L. Bubendorff, E. Beaurepaire, C. Mény, P. Panissod, and J. P. Bucher, Phys. Rev. B **56**, R7120 (1997); Appl. Phys. Lett. **83**, 7043 (1998).

[11] *Modern Electroplating*, edited by F. Lowenheim (Wiley, New York, 1974).

[12] E. Budevski, G. Staikov, and W. J. Lorenz, in *Electrochemical Phase Formation and Growth* (VCH, Weinheim, 1996).

[13] For a review, see W. Schwarzacher and H. Lashmore, IEEE Trans. Magn. **32**, 3133 (1996).

[14] K. D. Bird and M. Schlesinger, J. Electrochem. Soc. **42**, L65 (1995).

[15] P. Nallet, E. Chassaing, M. Walls, and M. H. J. Hÿtch, J. Appl. Phys. **79**, 6884 (1996).

[16] P. Nallet, E. Chassaing, A. Morrone, and J. E. Schmidt, J. Electrochem. Soc. (to be published).

[17] P. Allongue, H. Brune, and H. Gerischer, Surf. Sci. **275**, 414 (1992).

[18] L. Cagnon, V. Kieling, R. Cortes, and P. Allongue (unpublished).

[19] B. Voigtlander, G. Meyer, and N. M. Amer, Phys. Rev. B **44**, 10 354 (1991).

[20] S. Padovani, P. Molinas-Mata, F. Scheurer, and J. P. Bucher, Appl. Phys. A: Mater. Sci. Process. **66**, S1199 (1998).

[21] I. Sebastian, M. Heiler, K. Meinel, and H. Neddermeyer, Appl. Phys. A: Mater. Sci. Process. **66**, S525 (1998).

[22] S. Nakahara and S. Mahajan, J. Electrochem. Soc. **127**, 283 (1980).

[23] T. A. Tochiskii, A. V. Boltushkin, and V. G. Shadrov, Russ. J. Electrochem. **31**, 178 (1995).

[24] J. J. Rehr, Jpn. J. Appl. Phys., Part 1 **32**, 8 (1993).

[25] With $E_\perp$, Co atoms have only three out-of-plane neighbors at interfaces against six in the bulk of the layer. One may therefore normalize the amplitude of the EXAFS signal by multiplying it by $N/(N-1)$ where N is the number of atomic layer [N was derived from RBS, see Fig. 2(b)].

[26] N. Marsot, R. Belkou, H. Magnan, P. Le Fèvre, C. Guillot, and D. Chandesris, Phys. Rev. B **59**, 3135 (1999).

[27] D. M. Kolb, R. J. Randler, R. I. Wielgosz, and J. C. Ziegler, in *Electrochemical Synthesis and Modification of Materials*, edited by P. C. Andricacos, S. G. Corcoran, J. L. Delplancke, T. C. Moffat, and P. C. Searson, Symposia Proceedings No. 451 (Materials Research Society, Pittsburgh, 1997), p. 19.

[28] A. M. Bittner, J. Wintterlin, and G. Ertl, Surf. Sci. **376**, 267 (1997).

[29] W. Haiss and J. K. Sass, J. Electroanal. Chem. **386**, 267 (1995).

[30] The dimension of a Moiré pattern is given by $D=a_{\text{Au}}\cdot a_{\text{Co}}$ ($a_{\text{Au}}-a_{\text{Co}}$), where a's are lattice parameters. For bulk Co(0001) on Au(111)$D\sim19.5$ Å (Co-Co=2.51 Å and Au-Au=2.88 Å.

[31] *Constitution of Binary Alloys*, edited by M. Hansen (McGraw-Hill, New York, 1958); *Handbook of Binary Phase Diagrams* (Genium, Schenectady, NY, 1990).

[32] Ni grows epitaxially on Au(111) with nearly no internal strain since the Moiré is 20–21 Å on top of the second layer (Refs. 18 and 33). Correspondingly we find that Ni stripping does not leave nm islands on the Au surface (Ref. 18).

[33] F. Möller, O. Magnussen, and R. J. Behm, Phys. Rev. B **56**, 12 506 (1997).

[34] In the absence of external forces there is a z compression induced by a lateral stress ε_x: for a hcp layer $\varepsilon_z = -2(c_{13}/c_{33})\varepsilon_x$ where c_{ij} are elements of the tensor of strains. In the case of bulk cobalt $\varepsilon_z = 0.57\varepsilon_x$ (Ref. 35).

[35] J. F. Nye, in *Physical Properties of Crystals* (Oxford University Press, Oxford, 1967).

[36] *Cobalt Monograph* (Centre d'Information du Cobalt, Brussels, 1960).

[37] We measured the tunneling barrier on the Au(111) surface (1.66 eV) and on the Co bilayer (2.15 eV). Writing $i_{\text{tunnel}} \sim (\text{LDOS})\exp[-1.02\sqrt{\Phi}(\text{eV})s(\text{Å})]$, where symbols have their usual meaning, the expected *apparent* compression due to STM imaging (constant current mode) is $ds/s = -1/2(d\Phi/\sqrt{\Phi}) = 0.15$ in close agreement with observations.

[38] B. Dieny and A. Vedyayev, Europhys. Lett. **25**, 723 (1993).

[39] F. J. A. den Broeder, D. Kuiper, A. P. van de Mosselaer, and W. Hoving, Phys. Rev. Lett. **60**, 2769 (1988).

[40] G. H. O. Daalderpo, P. J. Kelly, and M. F. H. Schuurmans, Phys. Rev. B **50**, 9989 (1994).

[41] R. H. Victoria and J. M. MacLaren, Phys. Rev. B **47**, 11 583 (1993).

[42] O. Hosrtam, J. Trygg, J. M. Wills, B. Johansson, and O. Eriksson, Phys. Rev. B **53**, 9204 (1996).

[43] P. Bruno, J. Phys. F: Met. Phys. **18**, 1291 (1988).

[44] P. Bruno, J. Appl. Phys. **64**, 3153 (1988).

[45] N. Marsot, Ph.D. thesis, Université Paris-Sud, Orsay, 1999.

[46] C. Malière, D. Renard, and J. P. Chauvineau, Thin Solid Films **201**, 317 (1991); D. Renard and G. Nihoul, Philos. Mag. B **55**, 75 (1987).

[47] K. Hyomi, A. Murayama, J. Eickmann, and C. M. Flaso, J. Magn. Magn. Mater. **198–199**, 378 (1999).

[48] D. J. Srolovitz and J. P. Hirth, Surf. Sci. **255**, 111 (1991).

[49] J. V. Barth, H. Brune, G. Ertl, and R. J. Behm, Phys. Rev. B **42**, 9307 (1990).